Energy Engineering

Tech Science Press

https://doi.org/10.32604/ee.2026.076827

ARTICLE

# Optimization of Temperature Field Uniformity Induced by Heating-Element Configuration and Its Effect on Melting Rate of Phase Change Materials

**Hongtao Li**[1], **Liqiang Liang**[1], **Jiageng Li**[1], **Yunguang Ji**[1,*] **and Fuqiang Dong**[2]

[1]School of Mechanical Engineering, Hebei University of Science & Technology, Shijiazhuang, China
[2]Hebeisijian Construction Engineering Co., Ltd., Shijiazhuang, China

*Corresponding Author: Yunguang Ji. Email: jiyg@Hebust.edu.cn

Received: 27 November 2025; Accepted: 27 February 2026; Published: 12 November 2026

**ABSTRACT:** The configuration of multiple heat sources within a latent heat thermal energy storage (LHTES) unit directly influences the uniformity of the temperature field and profoundly affects the melting process of the phase change material (PCM). To investigate the impacts of heating-element configurations on temperature field homogenization and melting rate of paraffin in an LHTES unit, this study introduces a dimensionless scaling factor $\eta$ (defined as the ratio of the center-to-center distance between adjacent heating-element to the characteristic dimension of the container) and establishes a theoretical model for the optimal spacing of heating-element based on the Stefan condition. A combined approach of three-dimensional transient numerical simulation and experimental validation is employed to study the impact of heating-element configuration on melting efficiency in a 2 × 3 rectangular cylindrical-heating-element array. An experimental system with a measurement setup consisting of a 30-point thermocouple array and an infrared thermal imager was constructed to test and compare the temperature fields under different heating-element-distance $\Delta s$, respectively ($\Delta s$ = 30, 60, and 90 mm). The results show that, under equal power input, the unit achieves the shortest melting time at $\Delta s$ = 60 mm, which is 3.4% and 5.4% shorter than that at $\Delta s$ = 30 and 90 mm, respectively. A parallelogram array with a 45° misaligned angle further reduces the melting time by 5.2% compared to the rectangular array, Furthermore, an optimal scaling factor $\eta_{opt}$ = 0.34 is obtained, which reduces the melting time by 8.7% compared to the case of $\eta$ = 0.30. This study employs an integrated experimental and numerical approach to investigate how multiple heat-source configurations influence the melting process of phase-change materials (PCMs). The experimental results agree well with the simulation results, with a maximum relative deviation of 6.4%. This confirms the accuracy and engineering applicability of the numerical method, although some experimental uncertainties—particularly fluctuations in local temperature distributions—were observed. This study provides a quantitative basis for improving melting uniformity, and offers theoretical guidance to optimize structural compactness and heating-element configuration in LHTES units, which demonstrates promising practical applicability.

**KEYWORDS:** Latent heat thermal energy storage; heating-element configuration; temperature field uniformity; melting rate; optimal spacing

## 1 Introduction

The large-scale integration of renewable energy into the grid imposes increasingly stringent requirements on the peak regulation capability and operational flexibility of power systems. Latent heat thermal energy storage (LHTES) technology has emerged as a promising solution owing to its high energy density and nearly isothermal charging/discharging characteristics [1]. However, the inherent drawbacks of phase change materials (PCMs), including low thermal conductivity, delayed onset of natural convection, and uneven

Copyright © 2027 The Authors. Published by Tech Science Press. This work is licensed under a Creative Commons Attribution 4.0 International License, which permits unrestricted use, distribution, and reproduction in any medium, provided the original work is properly cited.

melting caused by thermal field interference under multi-heat-source conditions, have severely hindered the improvement of system power density and its practical engineering applications [2]. Currently, the core challenge in relevant research lies in how to effectively accelerate the melting rate of PCMs and achieve uniform temperature distribution, which is of great significance for the construction of efficient and reliable energy storage systems.

To overcome the thermal performance bottlenecks of PCMs, researchers worldwide have conducted systematic studies from the perspectives of structural design, flow regulation, and numerical modeling, gradually elucidating the mechanisms underlying heat transfer enhancement and melting homogenization. In terms of structural optimization, Pizzolato et al. [3] significantly increased the melting and solidification rates in LHTES units through topology-optimized fin design; Zhao et al. [4] investigated the influence of fin spacing on PCM melting rates and proposed optimized fin layouts, further validating the importance of fin design in heat transfer. Kasper et al. [5] explored the coupling relationship between natural convection and fin configuration, suggesting optimal fin spacing to enhance melting efficiency. Additionally, See et al. [6] designed heat sink structures considering natural convection through topology optimization, further revealing how natural convection promotes PCM melting rate. Meanwhile, other researchers have continued to optimize the melting performance and thermal conduction efficiency of PCM. Wang et al. [7] studied the thermal conduction effects of metal foam, topology-optimized fins, and their combinations, finding that metal foam structures more effectively improved PCM melting rates compared to traditional fins or combined structures, demonstrating significant heat transfer enhancement. In the broader context of geometric configuration research, Junaid et al. [8] systematically investigated the effect of inclination angle on the melting behavior of phase change materials (PCMs) by adopting a truncated double-cavity model. Their findings indicated that the natural convection was significantly enhanced at an inclination angle of 45°, accompanied by a more uniform temperature field distribution and an optimized melting rate, which provides valuable insights for the thermal performance optimization of PCMs in complex geometric structures.

Regarding flow control, Mosaffa et al. [9] employed an analytical model to investigate the moving boundary problem during the solidification process, revealing the influence of natural convection on PCM solidification. Marzouk et al. [10] conducted numerical simulations to study the effects of different fin geometries on the PCM melting process, proposing methods to optimize fin shapes for improved flow and heat transfer efficiency. Abhinand et al. [11] explored the relationship between melting time and the number of fins in fin-assisted systems, uncovering the non-monotonic impact of fin quantity on melting rates. Liu et al. [12] examined the influence of longitudinal fins on PCM melting performance, finding that fin configurations significantly improved the melting rate. Rawat et al. [13] effectively accelerated the PCM melting rate by employing flange fins in rectangular cavities and optimizing fin length and geometry. Mahdi et al. [14] emphasized the crucial role of natural convection in PCM melting process, highlighting that structural designs enhancing natural convection can substantially improve heat transfer efficiency.

In the context of geometric design and configuration, existing studies have shown that appropriately designing the shape and layout of fins on pipes plays a significant role in reducing the full melting time of PCM and enhancing heat transfer efficiency. Yang et al. [15] pointed out the notable impact of fin quantity on the full melting time, suggesting that a reasonable fin layout can effectively shorten the melting time. Zhang et al. [16] employed topology optimization methods to analyze the effect of reducing melting time and established an optimized relationship between rational heat source configuration and melting time. Ben Khedher et al. [17] introduced concave-convex fins, which improved internal convection and heat transfer within the PCM through their unique geometric shape, thereby accelerating the melting process.

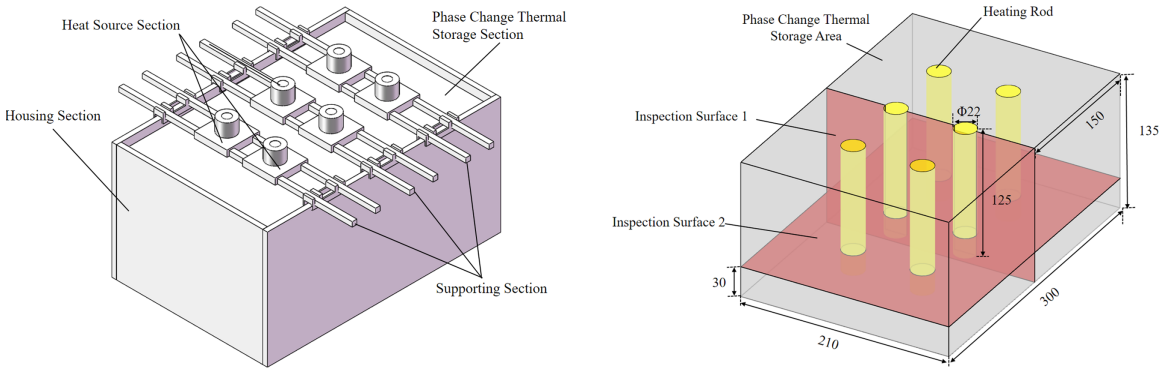
It is worth noting that the studies predominantly adopted the finite element method (FEM) for numerical simulations. To further improve the simulation accuracy of heat transfer processes—especially those involving strong temperature gradients, multi-heat-source interference, and transient phase change interfaces—the spectral element method (SEM), as a high-precision numerical approach, has exhibited remarkable advantages in the simulation of electromagnetic, acoustic, and thermal coupled fields. For instance, Mahariq et al. [18,19] found that in addressing acoustic and electromagnetic scattering problems, SEM outperforms traditional FEM in terms of accuracy and convergence when resolving high-frequency wave fluctuations and complex mode coupling. Beyond wave-related applications, recent advances in high-order spectral and discontinuous Galerkin spectral-element formulations have demonstrated strong convergence properties and high computational efficiency in large-scale wave propagation and coupled-field simulations [20]. In addition, the incorporation of absorbing boundary techniques, such as the perfectly matched layer (PML), has significantly enhanced their capability to handle open-boundary and large-domain problems by effectively reducing artificial reflections [21,22]. Modern spectral-element computational frameworks further provide scalable implementations and strong adaptability to complex geometrical configurations, which are essential for high-fidelity numerical simulations in real-world engineering applications [23]. This study primarily employs the finite element method for analysis, which demonstrates satisfactory accuracy. Based on the requirements of further research, future work will focus on the application and development of the generalized element method.

Based on the review of existing literature, several important research gaps remain in the application of PCMs in latent heat thermal energy storage (LHTES) systems: despite the abundance of numerical simulation achievements, experimental validation is relatively insufficient, which limits the model prediction accuracy and engineering reliability. Particularly under multi-heat-source configurations, the optimal configuration of heating elements and their impacts on temperature field uniformity and melting efficiency remain unclear. The key parameters, such as heat source configuration, spacing, and scaling factors, still lack a systematic optimization method. To address this, by combining numerical simulation with experimental validation, this study systematically investigates the effects of different heating-element configurations, heat source spacings, and optimal scaling factors on PCM melting behavior, and temperature field uniformity. This study establishes a solid quantitative foundation for enhancing melting uniformity in LHTES units and provides systematic theoretical guidance for optimizing both structural compactness and heating-element configuration, thereby significantly improving thermal performance, operational stability, and overall efficiency, and demonstrating strong potential for practical engineering applications.

## 2 Modeling and Methods

### *2.1 Models*

This study investigates a thermal energy storage (TES) unit using paraffin as the PCM, by developing a coupled physical model that integrates heat source configuration with heat transfer behavior, as shown in Fig. 1a. The model comprises four primary components: the phase change thermal storage (PCTS) region, the heat source, the support structure, and the casing, which is constructed of borosilicate glass with low thermal conductivity. The overall external dimensions of the TES unit are 312 mm × 222 mm × 156 mm ($X \times Y \times Z$), with a uniform wall thickness of 6 mm. Heat is supplied by vertically inserted cylindrical electric heaters with a diameter of 22 mm and a length of 160 mm. To accommodate the volumetric expansion of the phase change material (PCM) during the melting process, the container is intentionally not fully filled, leaving a reserved expansion space.




(a) Physical model (b) Simplified geometric model

**Figure 1:** Physical and simplified geometric models of the phase change thermal storage unit.

The corresponding simplified geometry is shown in Fig. 1b. The phase change thermal storage (PCTS) region has dimensions of 300 mm × 210 mm × 135 mm, and the heat sources are uniformly distributed within the PCTS region, with adjacent center-to-center spacings of 100 and 70 mm in the $X$ and $Y$ directions, respectively. Heat transfer from the heat sources is modeled as wall conduction. In order to characterize the temporal evolution of temperature and the melting behavior, two monitoring surfaces, 1 and 2, are defined at $x$ = 150 mm and $z$ = 30 mm, respectively.

### *2.2 Mathematical Model*

A balance equation is derived based on the coupled heat transfer between the thermal storage material and electric heaters. Given that the heat transfer within the PCTS region involves an internal heat source, the governing equation is established as follows [24]:

$$\rho c_p \frac{\partial T}{\partial t} = \frac{\partial}{\partial x}\left(k\frac{\partial T}{\partial x}\right) + \frac{\partial}{\partial y}\left(k\frac{\partial T}{\partial y}\right) + \frac{\partial}{\partial z}\left(k\frac{\partial T}{\partial z}\right) + \frac{W}{V_{\text{Heat}}} \tag{1}$$

where $\rho$ is the density of paraffin wax (kg·m$^{-3}$);$c_p$ is the specific heat capacity at constant pressure (J·kg$^{-1}$·K$^{-1}$); $T$ is the temperature (K); $t$ is the time (s); $k$ is the thermal conductivity of the phase change material (W·m$^{-1}$·K$^{-1}$); $q_v$ is the volumetric heat source (W·m$^{-3}$); $W$ is the power of the electric heater (W); $V_{\text{heat}}$ is the volume of the electric heater (m$^3$).

Since paraffin is uniformly distributed and continuous throughout the entire fluid domain, the continuity equation for this region is:

$$\frac{\partial p}{\partial \tau} + \nabla(\rho v) = 0 \tag{2}$$

where $v$ is the fluid velocity (m·s$^{-1}$)

Paraffin undergoes a phase change under the influence of an internal heat source, with its energy equation being [25]:

$$\frac{\partial(\rho T)}{\partial t} + \nabla\cdot\left(\rho\overline{U}T\right) = \nabla\cdot\left(\frac{\lambda}{c_p}\nabla T\right) + S_T \tag{3}$$

where $\lambda$ is the thermal conductivity of the fluid (W·m$^{-1}$·K$^{-1}$); $S_T$ is the source term.

The momentum equation is [26]:

$$\frac{\partial(\rho u)}{\partial t} + \nabla \cdot \left(\rho u \overline{U}\right) = \nabla \cdot (\mu \nabla u) - \frac{\partial P}{\partial x} + S_u \tag{4}$$

$$\frac{\partial(\rho v)}{\partial t} + \nabla \cdot \left(\rho v \overline{U}\right) = \nabla \cdot (\mu \nabla v) - \frac{\partial P}{\partial y} + S_v \tag{5}$$

$$\frac{\partial(\rho w)}{\partial t} + \nabla \cdot \left(\rho w \overline{U}\right) = \nabla \cdot (\mu \nabla w) - \frac{\partial P}{\partial z} + S_w \tag{6}$$

where $u$, $v$ and $w$ is the velocity component in the $x$, $y$ and $z$ direction, respectively; $S_u$, $S_v$ and $S_w$ is the momentum source term, respectively.

$$S_u = S_v = \frac{(1-\beta)^2}{\beta^3 + \eta} A_{\text{mush}} u \tag{7}$$

$$S_w = \frac{(1-\beta)^2}{\beta^3 + \eta} A_{\text{mush}} w - \left[1 - \alpha_v \left(T - T_{\text{ref}}\right)\right] \tag{8}$$

where $\beta$ is the liquid volume fraction; $\eta$ is the minimum value to prevent the denominator from being zero, usually ranging from $10^{-3}$ to $10^{-5}$; $A_{\text{mush}}$ is the mushy zone constant; $T_{\text{ref}}$ is the reference temperature (K); $\rho_{\text{ref}}$ is the density at the reference temperature (kg·m$^{-3}$); $\alpha_v$ is the coefficient of expansion (K$^{-1}$).

The isothermal electric heaters are arranged in an m × n grid pattern, aligned parallel to the edges of the casing with dimensions $X$ (length) × $Y$ (width). A scaling factor $\eta$ is defined as the ratio of the center-to-center distances, between adjacent heaters, $d_x$ and $d_y$, to the characteristic length of the corresponding edge. Thus, the relationship between heater spacing and casing dimensions is established as follows.

$$d_x = \eta X \; d_y = \eta Y \tag{9}$$

For a regular configuration, due to the symmetry of the temperature field, it can be considered that the temperature at the center point of an adjacent heat source is dominated by the 4 nearest heat sources, and the temperature gradient is:

$$\frac{\partial T}{\partial r} = 4 \frac{T_{\text{source}} - T_{\text{melt}}}{\sqrt{d_x^2 + d_y^2}} \tag{10}$$

where $T_{\text{source}}$ is the surface temperature of the electric heater (K); $T_{\text{melt}}$ is the melting temperature of the phase change material (K).

Define $\Delta T$ as the temperature difference between the surface of the electric heaters and the phase change material (PCM).

$$\Delta T = T_{\text{source}} - T_{\text{melt}} \tag{11}$$

The Stefan condition illustrates the principle governing the movement of the phase change interface, and is given as follows [27]:

$$\rho L \frac{dS}{dT} = \lambda \frac{\partial T}{\partial r} \tag{12}$$

where $\rho$ is the density of the phase change material (kg·m$^{-3}$); $L$ is the latent heat of phase change (J).

Assuming that the melting front moves from the surface of the electric heater to the center of the 4 heat sources, the Stefan condition is integrated and the temperature gradient obtained from temperature field superposition is substituted into the Eq. (12).

$$t_{\text{melt}} = \frac{\rho L d^2}{8\lambda \Delta T} \tag{13}$$

where $t_{\text{melt}}$ is the melting time (s).

A scaling factor is introduced to simplify Eq. (13), yielding the following expression:

$$t_{\text{melt}} = \frac{\rho L \eta^2 (X^2 + Y^2)}{8\lambda \Delta T} \tag{14}$$

When the heat sources are closely spaced, superposition arises in the temperature field; therefore, a correction term $c$ is introduced, and the melting-temperature expression can be rewritten as:

$$t_{\text{melt}} = K_s \left( \eta^2 + \frac{c}{\eta} \right) \tag{15}$$

$$K_s = \frac{\rho L (X^2 + Y^2)}{8\lambda \Delta T} \tag{16}$$

where $K_s$ is a simplified parameter, related to the physical properties of phase change materials and container dimensions; $c$ is an experimental calibration constant that requires an experimental determination.

By differentiating the Eq. (16) and setting the derivative to zero, the optimal spacing ratio $\eta_{opt}$ can be obtained:

$$\eta_{opt} = \left( \frac{c}{2} \right)^{1/3} \tag{17}$$

Therefore, after experimentally determining the melting time and scaling factor of paraffin, the values of $K_s$ and $c$ can be obtained using Eq. (15), and the optimal scaling factor $\eta_{opt}$ can ultimately be derived from Eq. (17).

### *2.3 Assumption*

To balance simulation accuracy and computational efficiency, appropriate simplifications are introduced, and the following assumptions are adopted [28]:

(1) Paraffin is uniformly distributed and homogeneous and isotropic, and no mass exchange with the external environment is considered;
(2) The density variation of paraffin satisfies the Boussinesq approximation, considering only temperature-induced density changes while neglecting the effects of other factors;
(3) The thermal resistance of the electric heaters is neglected.

Table 1 [29] shows paraffin physical properties used in this study.

**Table 1:** Physical properties of paraffin.

| Properties | Values |
|---|---|
| Phase change latent heat ($J \cdot kg^{-1}$) | 140,000 |
| Specific heat capacity ($J \cdot kg^{-1} \cdot K^{-1}$) | 2000 |
| Density ($kg \cdot m^{-3}$) | 850 |
| Thermal conductivity ($W \cdot m^{-1} \cdot K^{-1}$) | 0.2 |
| Phase-transition temperature (K) | 331 |

### *2.4 Meshing and Independence Verification*

In this model, the electric heater is vertically inserted into the phase change region. Therefore, during mesh generation process, the heaters section is removed, and the grids at the bottom of the removed section was structured with an O-grid topology, to achieve high grid quality. Since the electric heater acts as a heat source, the grids around it are refined to ensure simulation accuracy. The resulting grids at monitoring surface 1 are shown in Fig. 2.

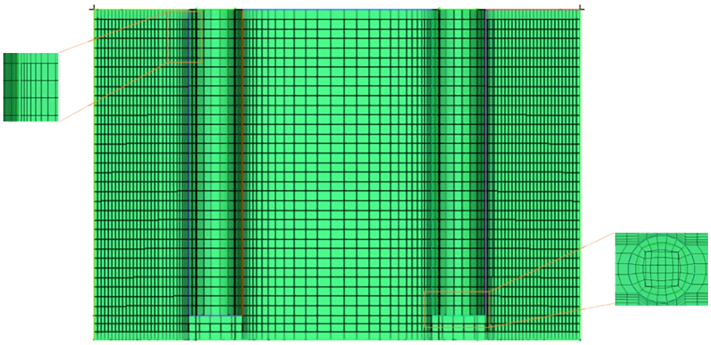


**Figure 2:** Grids on monitoring surface 1.

Monitoring points are selected on monitoring surface 1, with the temperature at these points when the liquid phase fraction reaches 20% serving as the criterion. Mesh sizes are divided into five levels: $N_1$ = 42,360, $N_2$ = 53,752, $N_3$ = 75,078, $N_4$ = 138,960, and $N_5$ = 198,144. Time steps of $t$ = 0.01, 0.1, and 1 s are selected for calculations. The temperatures at the monitoring points under different grid number were shown in Fig. 3. The figure indicates that when the grid number reaches 75,078, the temperature at the monitoring points shows slight variations with further increases in grid number, When the grid number reaches 138,960, the temperature at the monitoring points remains essentially unchanged. Considering the convergence, computational times and the computational accuracy, a grid number of 138,960 is ultimately selected for the numerical simulation, with a time step of 0.1 s.

### *2.5 Model Validation*

To validate the accuracy of the model, we apply the numerical simulation method developed in this paper to simulate the experiment in the reference [30]. Boundary conditions and three temperature measurement layers identical to those in the experiment were set. The validation results are shown in Fig. 4. The maximum deviation between the simulation results and experimental data of the upper layer was 6.1%, while the maximum deviations for the middle and lower layers were 7.2% and 5.6%, respectively. Although the simulation results obtained using the proposed simulation method differ slightly from the experimental

results, the discrepancies are minor and the overall trends are consistent, which validates the accuracy and applicability of proposed simulation method.

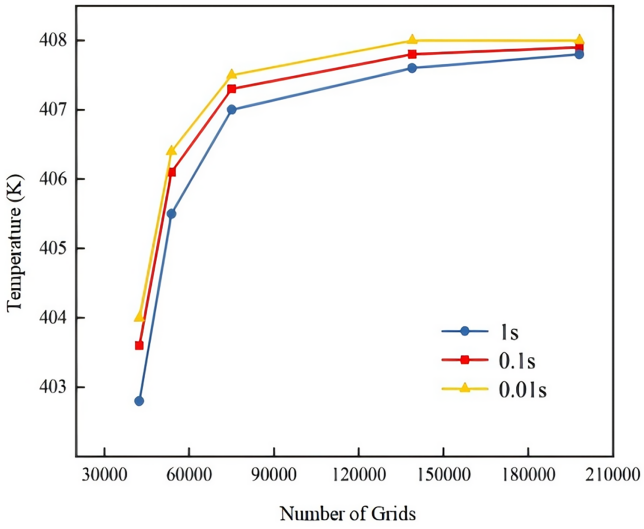



**Figure 3:** Verification of grid independence.

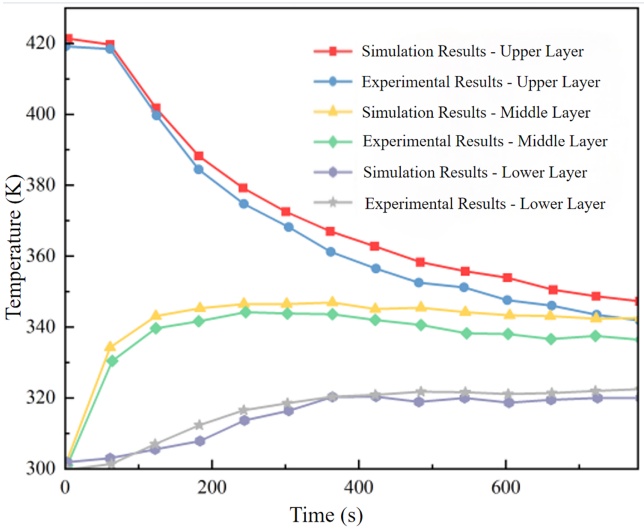



**Figure 4:** Model accuracy validation.

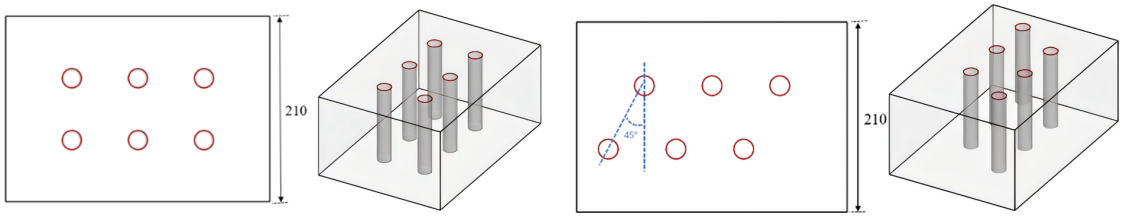
## 3 Results and Analysis

### *3.1 Melting Efficiency*

Two configurations of heat sources array are proposed to examine how the spatial distribution of heat sources affects the PCM melting rate. Fig. 5a illustrates the rectangular array of heaters, while Fig. 5b illustrates the parallelogram array with a 45° misalignment angle between adjacent rows.

As shown in Fig. 6, during the initial stage (250–500 s), the melting process is mainly governed by heat conduction, with the heating-elements acting as localized heat sources, resulting in discrete liquid regions. In the intermediate stage (500–750 s), adjacent liquid regions gradually merge, which enhances natural

convection and significantly accelerates the expansion of the liquid phase. In the later stage (750–1000 s), the liquid phase becomes dominant, and the melting rate is progressively limited by the heat transfer conditions at the boundaries. Compared with the rectangular array, the parallelogram array exhibits a thicker liquid layer near the boundaries. This behavior can be attributed to the closer proximity of the array elements to the boundaries and the enhanced flow-induced convection. Consequently, the parallelogram array configuration promotes a more uniform expansion and earlier interconnection of the liquid regions, thereby improving the overall melting efficiency.




(**a**) Rectangle array (**b**) Parallelogram array

**Figure 5:** Two configurations of heat sources array.

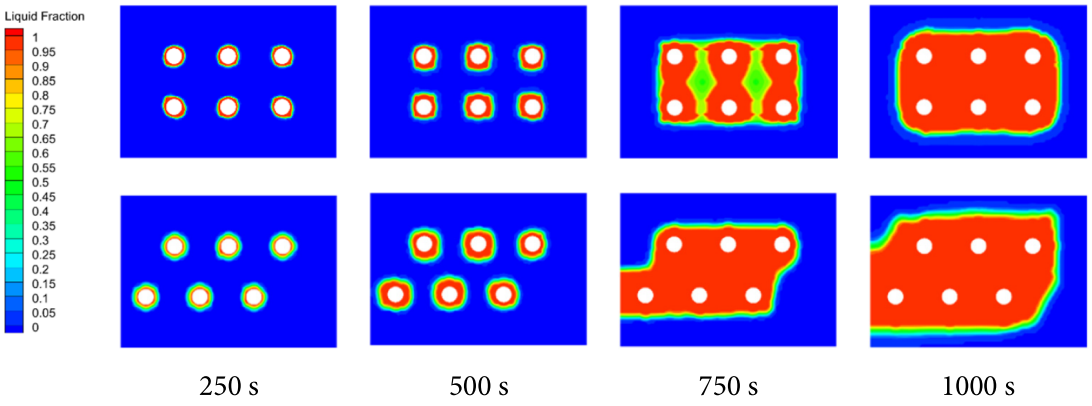



**Figure 6:** Liquid fraction evolution on monitoring surface 2 for different array.

As shown in Fig. 7, both arrays exhibit similar initial melting trends during the heat-conduction-dominated stage, indicating that the early evolution of the liquid fraction is only marginally influenced by the array configuration. Owing to the aligned superposition of heat sources, the rectangular array exhibits a slightly higher liquid fraction growth rate in the early stage. However, as the melting progresses and natural convection becomes increasingly dominant, the parallelogram array effectively mitigates excessive thermal superposition and enhances heat transfer through its staggered arrangement. This promotes stronger convective motion and accelerates the overall melting process. As a result, the total melting time is reduced from 1710 to 1625 s, corresponding to a decrease of approximately 5.2%.

Fig. 8 indicates that within the time interval of 600–1500 s, the rectangular array exhibits a higher rate of temperature rise but a slower melting process, implying that a larger portion of the input heat is converted into sensible heat rather than latent heat. This behavior can be attributed to the superposition of thermal plumes generated by the aligned heat sources, which constrains fluid motion, induces localized heat accumulation, and leads to insufficient thermal mixing. In contrast, the parallelogram array enhances cross-region heat transfer by redirecting convective flow through heat source misalignment. This effectively

mitigates local overheating and heat accumulation, thereby promoting stronger natural convection and accelerating liquid phase growth.

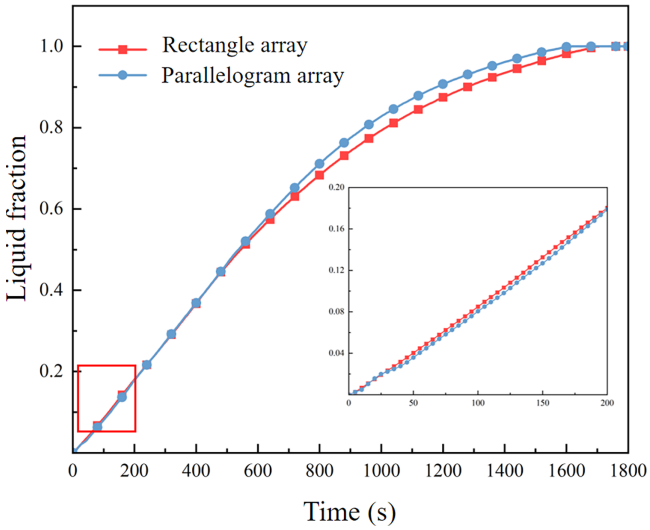



**Figure 7:** Liquid fraction variation curves for different array of heat sources.

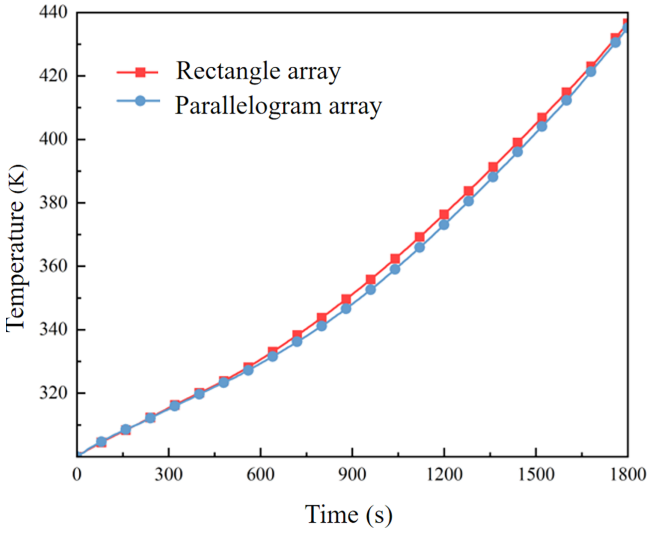



**Figure 8:** Temperature variation curves for different array.

### *3.2 Optimization of Heat Source Spacing*

Although the parallelogram configuration demonstrates superior melting performance compared with the rectangular one, the optimization of heat source spacing was first conducted under a regular rectangular configuration. This approach was chosen because the rectangular array provides a symmetric and analytically tractable reference structure, facilitating the derivation of a theoretical model for optimal spacing based on temperature field superposition and the Stefan condition. The resulting optimal spacing ratio thus serves as a baseline design criterion, upon which further structural optimization—such as the introduction of misalignment—can be applied to achieve additional enhancement.

To investigate the impact of heat source spacing on heat accumulation, a six-heater array with equal distances in both the $x$ and $y$ directions was constructed. The adjacent center-to-center distance, $\Delta s$, was treated as the control variable, with three cases considered: $\Delta s$ = 30, 60, and 90 mm, as shown in Fig. 9.

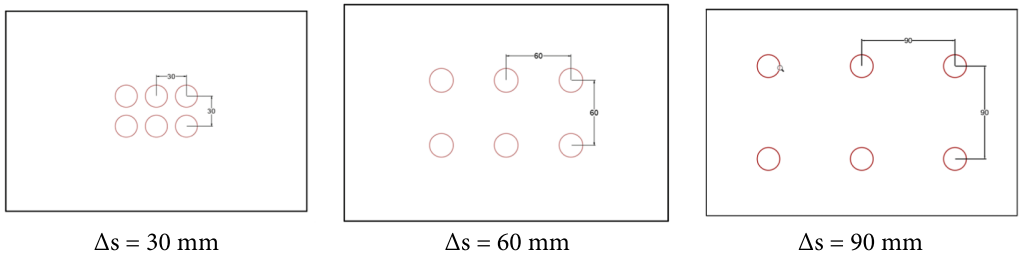



**Figure 9:** Heat sources schematic ($z$-direction) for various spacing conditions.

Fig. 10 illustrates the temporal evolution of the liquid fraction on Monitoring Surface 2 under different heat source spacings. In the early stage, melting occurs locally around each heat source and is minimally influenced by spacing. As melting progresses, the influence of spacing becomes pronounced. When $\Delta s$ = 30 mm, excessive thermal-field overlap leads to rapid melting in the central region but impedes outward heat diffusion. Conversely, when $\Delta s$ = 90 mm, the weak interaction between adjacent heat sources delays the coalescence of liquid regions and overall melting. An intermediate spacing of $\Delta s$ = 60 mm achieves a balanced thermal-field distribution, promotes uniform liquid-phase expansion, and facilitates the development of natural convection, resulting in the most efficient melting process.

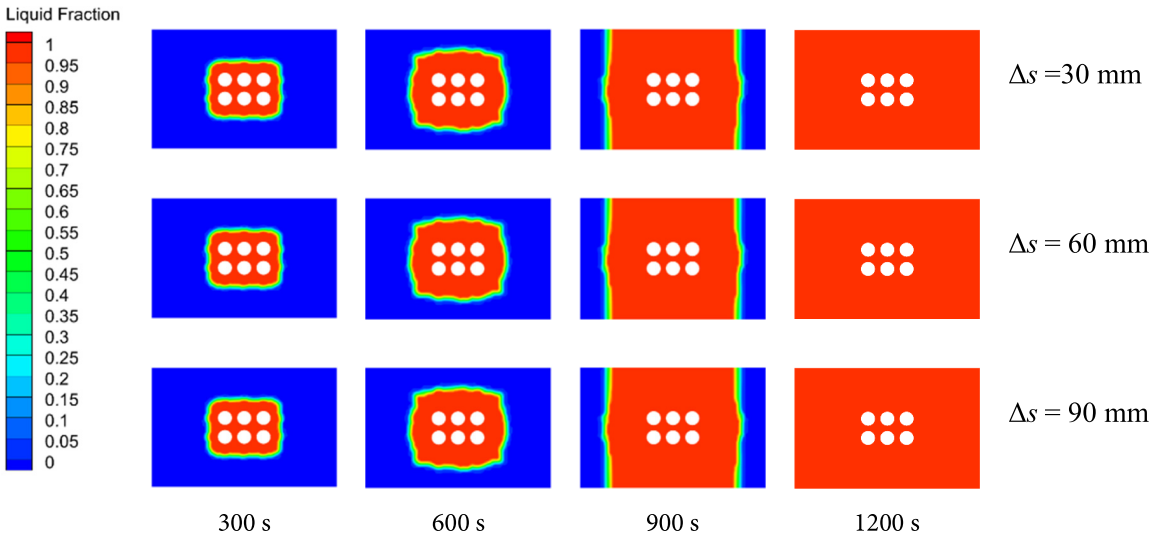



**Figure 10:** Liquid fraction evolution on monitoring surface 2 under different heat source spacings.

Fig. 11 illustrates the evolution of the liquid fraction under different heat source spacings. In the early stage, the liquid fraction increases at a nearly identical rate for all cases, indicating a conduction-dominated melting process. As melting proceeds, distinct differences emerge. The intermediate spacing of $\Delta s$ = 60 mm exhibits the highest liquid fraction growth rate, particularly during the convection-dominated stage, leading to the shortest overall melting time. In contrast, excessively small or large spacings result in thermal-field overlap or insufficient interaction between heat sources, respectively, both of which impede efficient melting.

These results confirm the existence of an optimal heat source spacing that maximizes latent heat utilization and melting efficiency.

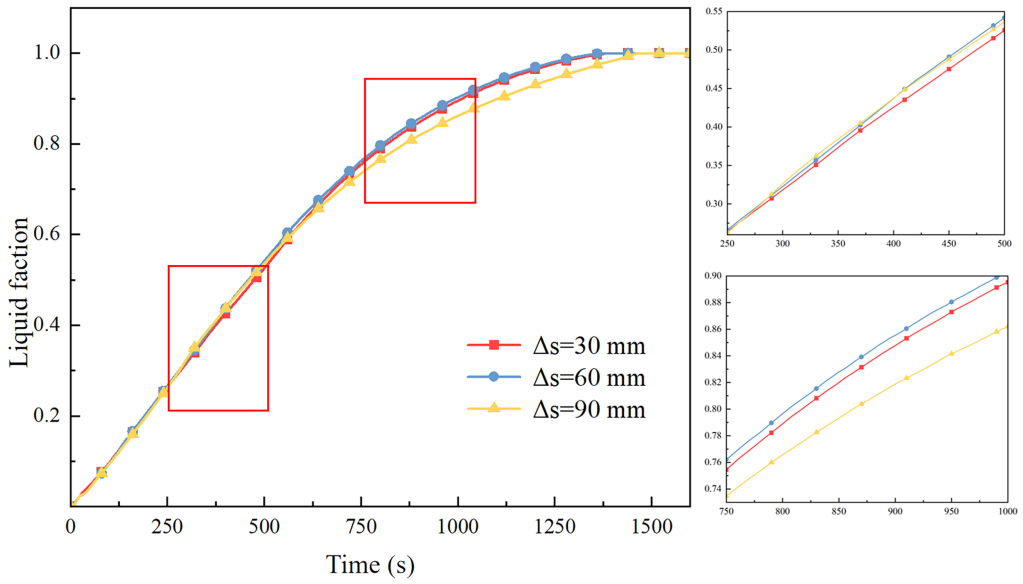



**Figure 11:** Liquid fraction evolution curves at different heat source spacings.

Fig. 12 presents the temperature variation curves under different heat source spacings. During the early stage, the temperature evolution is nearly identical for all cases, indicating a conduction-dominated heat transfer regime. As melting proceeds, noticeable differences emerge. The case with $\Delta s$ = 90 mm exhibits the highest temperature rise due to weak thermal interaction and delayed onset of natural convection, Conversely, the case with $\Delta s$ = 30 mm shows moderate temperature growth influenced by localized heat accumulation. In contrast, the intermediate spacing of $\Delta s$ = 60 mm consistently maintains the lowest temperature level, suggesting that a larger fraction of the input heat is effectively utilized for latent heat absorption. This behavior further confirms that $\Delta s$ = 60 mm provides the most efficient melting performance.

### *3.3 Verification of the Optimal Spacing Ratio $\eta_{opt}$*

Based on the simplified parameter $K_s$ and the experimentally calibrated constant c, the optimal scaling factor $\eta_{opt}$ can be determined. Numerical simulations were performed in conjunction with the governing expressions to evaluate $\eta_{opt}$ under the calibration conditions. To validate the proposed approach, experiments were conducted under three operating conditions, in which the scaling factor $\eta$ was set to 0.4, 0.3, and 0.2, respectively, with the heat sources arranged in a 2 × 3 array.

Fig. 13 illustrates the evolution of the liquid fraction under different scaling factors. In the early stage, the liquid fraction increases almost identically for all cases, indicating a conduction-dominated melting process. As melting proceeds, noticeable differences emerge. Among the tested conditions, $\eta$ = 0.3 exhibits the highest liquid fraction growth rate and the shortest melting time. In contrast, excessively small or large values of $\eta$ lead to thermal-field overlap or insufficient interaction between heat sources, respectively, both of which hinder efficient melting. These results confirm the existence of an optimal scaling factor that maximizes latent heat utilization and melting efficiency.

Based on the scaling factors values $\eta$ and the corresponding melting times $t$ obtained from the three operating conditions, the optimal scaling factor $\eta_{opt}$ = 0.34 was determined by combining Eqs. (13)–(17).

Under this optimal condition, the heat source spacings in the $x$ and $y$ directions are $d_x$ = 102 mm and $d_y$ = 71.4 mm, respectively. To verify the melting performance of paraffin at $\eta_{opt}$ = 0.34, a comparative analysis was conducted between this optimal configuration and the case with $\eta$ = 0.3.

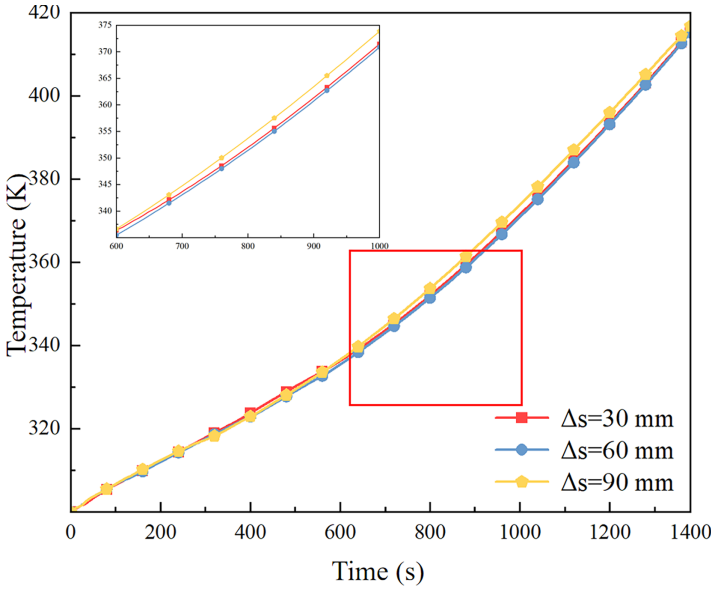



**Figure 12:** Temperature variation curves at different heat source spacing.

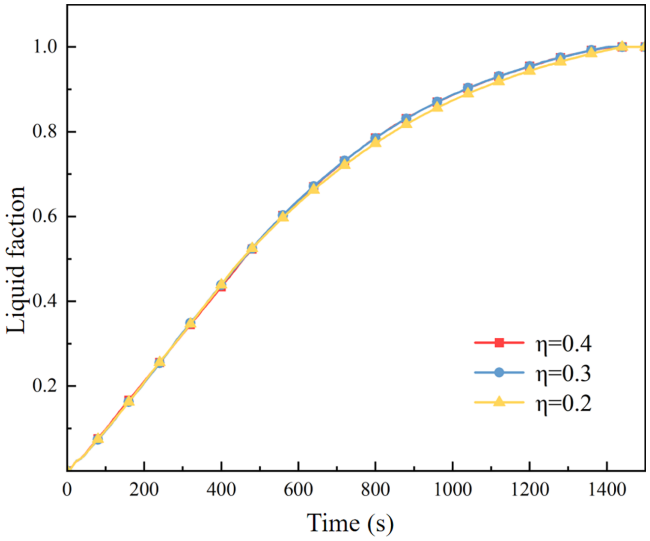



**Figure 13:** Liquid fraction evolution curves at different scaling factors.

Fig. 14 compares the liquid fraction evolution for $\eta$ = 0.3 and the theoretically predicted optimal value $\eta$ = 0.34. In the early stage, both cases exhibit similar melting behavior, indicating a conduction-dominated regime. As melting progresses, the case with $\eta$ = 0.34 consistently shows a higher liquid fraction and a steeper growth rate, particularly during the intermediate stage. This behavior can be attributed to the optimized heat source spacing, which enhances liquid-phase connectivity and promotes stronger natural convection.

Consequently, the melting time is further reduced, confirming the effectiveness of the proposed optimal scaling factor.

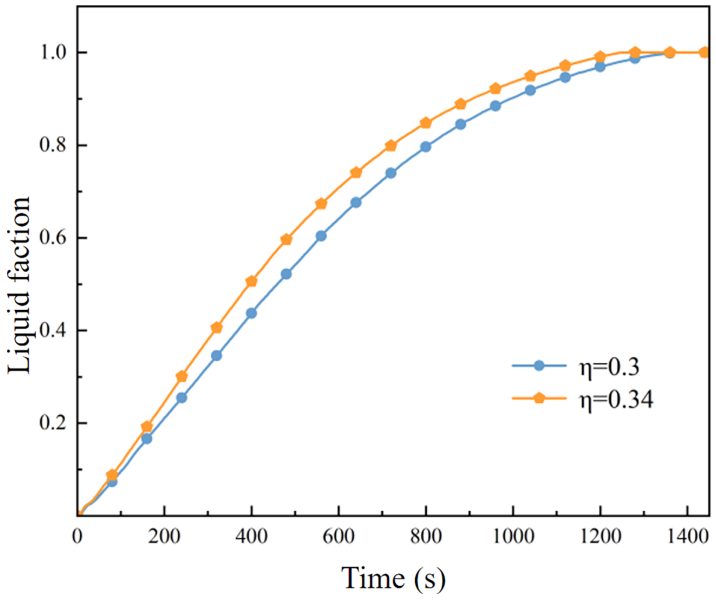



**Figure 14:** Liquid fraction evolution vs. time curves at $\eta$ = 0.3 and $\eta$ = 0.34.

## 4 Experimental Research

### *4.1 Experimental System and Equipment*

The experimental system for latent heat thermal energy storage research is composed of three core subsystems: a temperature controller, a phase-change apparatus, and a temperature measurement system, as illustrated in Fig. 15. For accurate temperature data acquisition, a high-precision 32-channel temperature data recorder, calibrated K-type thermocouples, and a high-resolution infrared thermal imaging camera are employed.

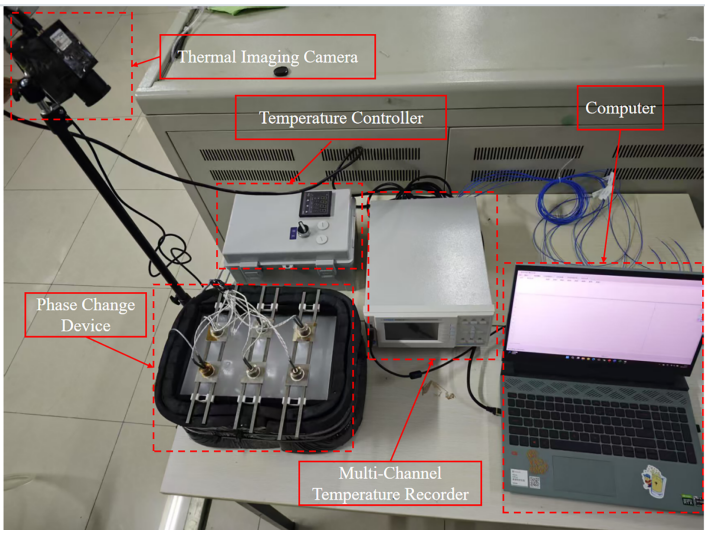



**Figure 15:** Experimental system.

### *4.2 Data Processing Method*

During the experiment, transient temperatures are measured and recorded using the temperature recorder and the infrared thermal imaging camera. Concurrently, the liquid fraction of the paraffin is reconstructed using a validated formula-based post-processing method. To achieve high-fidelity monitoring of temporal temperature evolution, a total of 30 thermocouples are embedded in the paraffin, distributed across five horizontal layers with six measurement points per layer, as shown in Fig. 16, where the five layers were uniformly spaced at 22.5 mm intervals along the vertical direction from the bottom to the top.

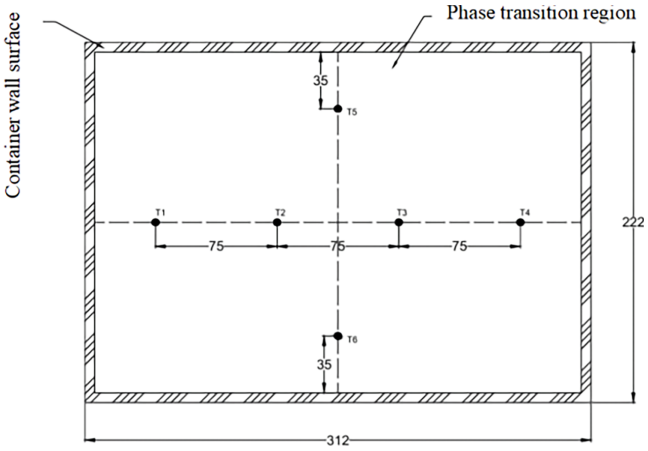



**Figure 16:** Temperature measurement points on each layer.

### *4.3 Experimental Procedures*

The experimental procedure consists of three steps, PCM preparation, preprocessing, experiment conduction, and data processing, as shown in Fig. 17.

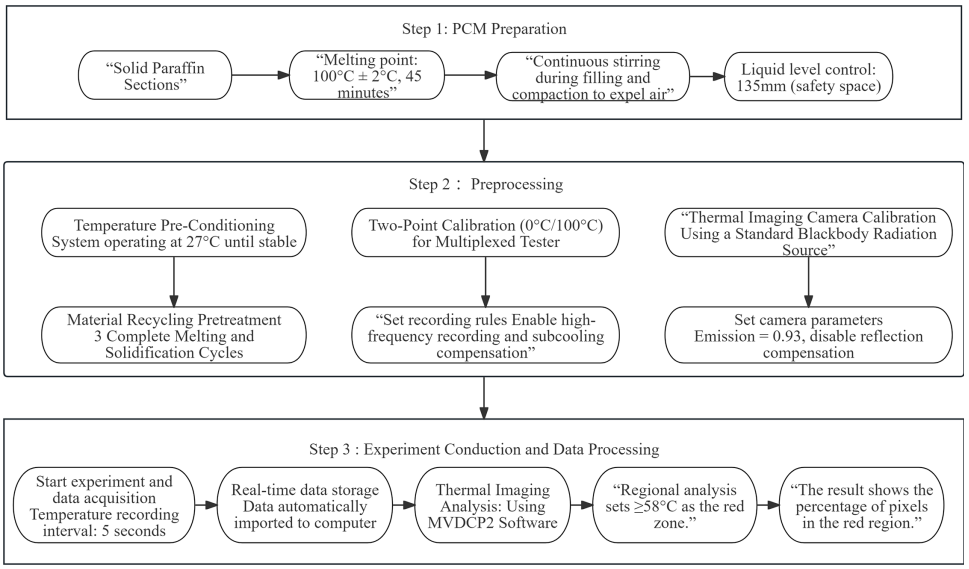



**Figure 17:** Experimental procedures.

### *4.4 Experimental Verification*

Fig. 18 compares the temperature histories obtained from numerical simulations and experiments at three representative measurement points ($T_1$, $T_2$, and $T_5$). The simulated results agree well with the experimental data in terms of overall trends and characteristic stages, including the initial heating phase, the phase-change plateau, and the subsequent temperature rise in the liquid-dominated regime. Among the three points, $T_2$, which is closest to the heat source, exhibits the highest temperature and the strongest convective heat transfer, with minimal deviation between the simulation and the experiment. The maximum relative deviation for all measurement points remains below 6.4%, indicating that the proposed numerical model is sufficiently accurate and reliable for predicting the melting behavior of the PCM.

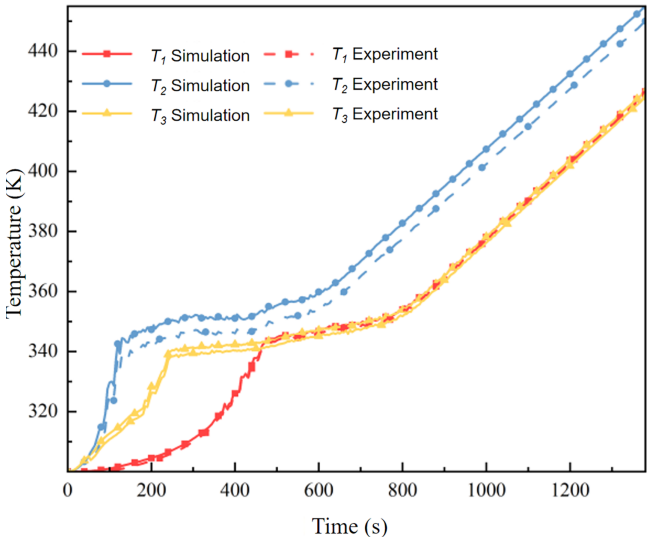



**Figure 18:** Comparison of simulation results and experimental results.

Based on the coupled effects of heat conduction and phase-change kinetics, a theoretical model for the optimal scaling factor $\eta_{opt}$ in a symmetrically arranged configuration is proposed, and its quantitative relationship with the melting time is derived. The theoretical model indicates that melting efficiency is optimal when $\eta_{opt}$ = 0.34. The optimal thermal field distribution at $\eta_{opt}$ = 0.34 arises from an optimized heat source configuration and the full utilization of natural convection. The critical threshold spacing between heat sources minimizes ineffective overlap in the thermal field, prevents localized thermal accumulation, and ensures continuous thermal coverage. Simultaneously, this spacing enables synergistic lifting of adjacent thermal plumes during their mid-to-late development stages, thereby enhancing overall convective intensity. It avoids flow interference caused by excessively narrow spacing or convective isolation resulting from overly wide spacing. This facilitates earlier and more complete dominance of natural convection as the primary heat transfer mechanism, significantly accelerating the advance of the melting front. Consequently, this ratio achieves an optimal balance between fluid kinetic energy dissipation and heat transport efficiency, resulting in more uniform temperature distribution and optimal energy storage performance. It provides a universal quantitative design criterion for the configuration of heat sources in phase change energy storage systems.

To validate the proposed model, experiments were conducted under conditions of $\eta$ = 0.4, 0.3, and 0.2, with the melting curves presented in Fig. 19. The experimental trends exhibit a good agreement with the simulation results. However, the experimental liquid fraction demonstrates a slower initial increase and

a longer final melting time, which are likely due to convective heat loss from the container walls to the ambient air.

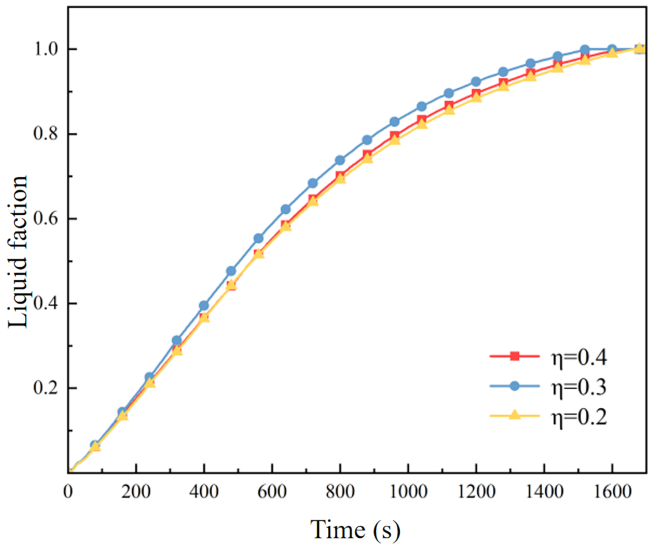



**Figure 19:** Liquid fraction evolution curve obtained by experiments for different scaling factors.

Fig. 20 presents the experimentally measured evolution of the liquid fraction for $\eta$ = 0.3 and $\eta$ = 0.34. Both cases exhibit a monotonic increase in liquid fraction over time; however, the configuration with $\eta$ = 0.34 consistently achieves a higher liquid fraction throughout the melting process. In particular, during the intermediate stage, the growth rate of the liquid phase is noticeably enhanced. As a result, the total melting time is reduced from 1535 to 1415 s, corresponding to a decrease of approximately 7.8%. These experimental results are in good agreement with the numerical predictions, confirming the validity of the proposed optimal scaling factor.

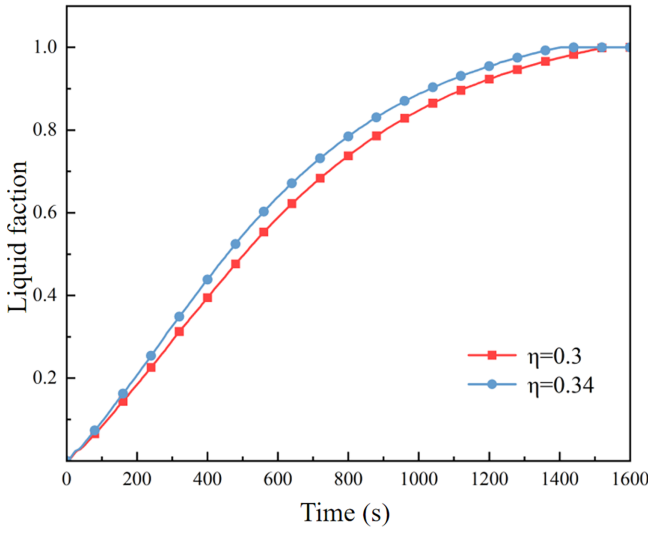



**Figure 20:** Liquid fraction curves obtained by experiments for $\eta$ = 0.3 and 0.34.

## 5 Conclusions

To investigate the effects of heat source spacing and configuration on the uniformity of phase change heat storage and the melting rate of paraffin, a theoretical model for the optimal heat source spacing was developed based on the dimensionless scaling factor $\eta$. A numerical approach integrating three-dimensional transient simulations with experimental validation was employed, leading to the following conclusions:

(1) Under constant power input conditions, an optimal heat source spacing range is observed. Numerical simulations demonstrate that a heat source spacing of $\Delta s$ = 60 mm yields the minimum melting time of 1390 s, representing reductions of 3.4% and 5.4% relative to the cases with $\Delta s$ = 30 mm and $\Delta s$ = 90 mm, respectively.

(2) Compared to symmetrical configurations, the parallelogram array with a 45° misalignment angle effectively prevents thermal plume superposition along the same line and improves natural convection channels, thereby further reducing the melting time by approximately 5.2%.

(3) The results indicate that the parallelogram array significantly improves temperature-field uniformity during PCM melting. By avoiding thermal plume superposition and enhancing flow-induced convection, the parallelogram configuration promotes more uniform heat distribution and liquid-phase expansion. In contrast, the rectangular array suffers from localized heat accumulation, leading to higher temperatures but reduced latent heat utilization.

(4) Based on numerical simulations and experimental calibration, the optimal scaling factor $\eta_{opt}$ = 0.34 is obtained. Compared to the $\eta$ = 0.3 operating condition, this optimal factor further reduces melting time by 8.7% in numerical simulations and 7.8% in experiments, significantly enhancing melting efficiency.

(5) This study establishes a quantitative guideline ($\eta_{opt}$ = 0.34) for a specific 2 × 3 array, and future work should explore the universality of this factor across different heat source quantities (e.g., 3 × 3 and 4 × 4 arrays), container geometries, and various PCMs with distinct thermophysical properties. Future work should integrate dynamic power control with optimized layouts and extend the approach to multi-objective optimization, balancing melting rate, structural compactness, and energy efficiency in advanced LHTES systems.

**Acknowledgement:** We sincerely thank all the faculty and staff of the School of Mechanical Engineering of Hebei University of Science and Technology for their close cooperation and strong support during our research period.

**Funding Statement:** This work was supported by the Major Support Project in Hebei Province (grant number: 24294501Z).

**Author Contributions:** The author's contribution to this manuscript is declared as follows: Research conception and design: Hongtao Li; Data Collection: Liqiang Liang; Result Analysis and Interpretation: Jiageng Li; Experimental platform construction and organization of related data and figures: Fuqiang Dong; Manuscript review and editing, academic guidance: Yunguang Ji; First draft written by Liqiang Liang. All authors reviewed and approved the final version of the manuscript.

**Availability of Data and Materials:** The data on which the results of this study are based can be obtained from the corresponding author, Yunguang Ji, upon reasonable request.

**Ethics Approval:** Not applicable.

**Conflicts of Interest:** The authors declare no conflicts of interest.

## References


1. Xu B, Li P, Chan C. Application of phase change materials for thermal energy storage in concentrated solar thermal power plants: a review to recent developments. Appl Energy. 2015;160(9):286–307. doi:10.1016/j.apenergy.2015.09.016.
2. Liu C, Xu D, Weng J, Zhou S, Li W, Wan Y, et al. Phase change materials application in battery thermal management system: a review. Materials. 2020;13(20):4622. doi:10.3390/ma13204622.
3. Pizzolato A, Sharma A, Maute K, Sciacovelli A, Verda V. Design of effective fins for fast PCM melting and solidification in shell-and-tube latent heat thermal energy storage through topology optimization. Appl Energy. 2017;208:210–27. doi:10.1016/j.apenergy.2017.10.050.
4. Zhao C, Wang J, Sun Y, He S, Hooman K. Fin design optimization to enhance PCM melting rate inside a rectangular enclosure. Appl Energy. 2022;321(4):119368. doi:10.1016/j.apenergy.2022.119368.
5. Kasper L, Pernsteiner D, Koller M, Schirrer A, Jakubek S, Hofmann R. Numerical studies on the influence of natural convection under inclination on optimal aluminium proportions and fin spacings in a rectangular aluminium finned latent-heat thermal energy storage. Appl Therm Eng. 2021;190:116448. doi:10.1016/j.applthermaleng.2020.116448.
6. See YS, Ho JY, Leong KC, Wong TN. Experimental investigation of a topology-optimized phase change heat sink optimized for natural convection. Appl Energy. 2022;314:118984. doi:10.1016/j.apenergy.2022.118984.
7. Wang S, Hou X, Yin J, Xing Y, Wang Z. Comparative study of the thermal enhancement for spacecraft PCM thermal energy storage units. Aerospace. 2022;9(11):705. doi:10.3390/aerospace9110705.
8. Junaid M, Saha G, Shahrear P, Saha SC. Phase change material performance in chamfered dual enclosures: exploring the roles of geometry, inclination angles and heat flux. Int J Thermofluids. 2024;24:100919. doi:10.1016/j.ijft.2024.100919.
9. Mosaffa AH, Talati F, Tabrizi HB, Rosen MA. Analytical modeling of PCM solidification in a shell and tube finned thermal storage for air conditioning systems. Energy Build. 2012;49:356–61. doi:10.1016/j.enbuild.2012.02.053.
10. Marzouk SA, Aljabr A, Almehmadi FA, Sharaf MA, Alam T, Dobrotă D. Thermal performance enhancement of phase change material melting using innovative fins. Therm Sci Eng Prog. 2025;61:103585. doi:10.1016/j.tsep.2025.103585.
11. Abhinand S, Sharma A, Kothadia HB. Performance analysis of PCM melting in a fin-assisted thermal energy storage system—a numerical study. Int Commun Heat Mass Transf. 2023;144:106747. doi:10.1016/j.icheatmasstransfer.2023.106747.
12. Liu HY, Qu BC, Wu CM, Li YR. Numerical study of PCM melting performance in a rectangular container with various longitudinal fin structures. J Energy Storage. 2024;94(5):112529. doi:10.1016/j.est.2024.112529.
13. Rawat P, Ashwni, Sherwani AF. A numerical study on the impact of fin length arrangement and material on the melting of PCM in a rectangular enclosure. Int J Heat Mass Transf. 2023;205:123932. doi:10.1016/j.ijheatmasstransfer.2023.123932.
14. Mahdi MS, Mahood HB, Campbell AN, Khadom AA. Natural convection improvement of PCM melting in partition latent heat energy storage: numerical study with experimental validation. Int Commun Heat Mass Transf. 2021;126(10):105463. doi:10.1016/j.icheatmasstransfer.2021.105463.
15. Yang X, Wang X, Liu Z, Luo X, Yan J. Effect of fin number on the melting phase change in a horizontal finned shell-and-tube thermal energy storage unit. Sol Energy Mater Sol Cells. 2022;236(2):111527. doi:10.1016/j.solmat.2021.111527.
16. Zhang Z, Chen X, Zhang N, Yuan Y, Dzhonova-Atanasova D, Attia S. Optimal design and performance investigation of latent heat thermal energy storage system integrated with nonuniformed topology fins. J Energy Storage. 2025;121(2):116564. doi:10.1016/j.est.2025.116564.
17. Ben Khedher N, Mahdi JM, Majdi HS, Khosravi K, Al-Azzawi WK, Al-Qrimli FA, et al. CFD analysis of phase-change material-based heat storage with dimple-shaped fins: evaluation of fin configuration and distribution pattern. J Comput Des Eng. 2022;9(5):2055–72. doi:10.1093/jcde/qwac105.
18. Mahariq I, Giden IH, Alboon S, Aly WHF, Youssef A, Kurt H. Investigation and analysis of acoustojets by spectral element method. Mathematics. 2022;10(17):3145. doi:10.3390/math10173145.

19. Mahariq I, Kurt H, Kuzuoğlu M. Questioning degree of accuracy offered by the spectral element method in computational electromagnetics. Appl Comput Electromagn Soc J. 2015;30(7):698–705. doi:10.7763/ijcte.2014.v6.916.
20. Liu QQ, Zhuang M, Zhan W, Shi L, Liu QH. A hybrid implicit-explicit discontinuous Galerkin spectral element time domain (DG-SETD) method for computational elastodynamics. Geophys J Int. 2023;234(3):1855–69. doi:10.1093/gji/ggad168.
21. Buntin LM, Kalscheuer T, Kreiss G, Ren Z. Improved accuracy of plane-wave electromagnetic modelling by application of the total and scattered field decomposition and perfectly matched layers. Geophys J Int. 2023;235(2):1201–17. doi:10.1093/gji/ggad264.
22. Luo Y, Wang T, Li Y, Cai J, Wang Y, Fang G. A residual perfectly matched layer for wave propagation in elastic media. Acta Geophys. 2024;72(3):1561–73. doi:10.1007/s11600-023-01145-x.
23. Massaro D, Peplinski A, Stanly R, Mirzareza S, Lupi V, Mukha T, et al. A comprehensive framework to enhance numerical simulations in the spectral-element code Nek5000. Comput Phys Commun. 2024;302(3):109249. doi:10.1016/j.cpc.2024.109249.
24. Tsega EG. A numerical solution of three-dimensional unsteady state heat equation. Int J Math Model Comput. 2021;11(1):49–60.
25. Tao WQ. Chapter 2 governing equations and initial-boundary conditions. In: Numerical heat transfer. 2nd ed. Xi'an, China: Xi'an Jiaotong University Press; 2001. (In Chinese).
26. White FM. Chapter 6 viscous flow in ducts, chapter 12 compressible flow. In: Fluid mechanics. 8th ed. New York, NY, USA: McGraw-Hill Education; 2015.
27. Yang SM, Tao WQ. Heat transfer. 5th ed. Beijing, China: Higher Education Press; 2019. p. 112–5. (In Chinese).
28. Faraji M, El Qarnia H. Numerical study of melting in an enclosure with discrete protruding heat sources. Appl Math Model. 2010;34(5):1258–75. doi:10.1016/j.apm.2009.08.012.
29. Mao S, Liu Y, Wu X, Zhang L, Chen J, Zhou T. Thermal energy storage performance, application and challenge of phase change materials: a review. Energy Storage Sav. 2025;4(3):300–22. doi:10.1016/j.enss.2025.03.001.
30. Li Y. Experimental and numerical study on the heat transfer performance of a single-tank paraffin thermal energy storage system [master's thesis]. Wuhan, China: Wuhan University of Science and Technology; 2021. (In Chinese).